Compact Ionized Gas Region Surrounded by Porous Neutral Gas in a Dusty Lyman Break Galaxy at Redshift z = 8.312

(article starts on next page)

Compact Ionized Gas Region Surrounded by Porous Neutral Gas in a Dusty Lyman Break Galaxy at Redshift $z = 8.312$

Masato Hagimoto[1] , Yoichi Tamura[1] , Akio K. Inoue[2,3] , Hideki Umehata[4,1] , Tom J. L. C. Bakx[5] ,
Takuya Hashimoto[6,7] , Ken Mawatari[3] , Yuma Sugahara[2] , Yoshinobu Fudamoto[8] , Yuichi Harikane[9] ,
Hiroshi Matsuo[10,11] , and Akio Taniguchi[12,1]

[1] Department of Physics, Graduate School of Science, Nagoya University, Furo, Chikusa, Nagoya, Aichi 464-8602, Japan; hagimoto@a.phys.nagoya-u.ac.jp
[2] Department of Physics, School of Advanced Science and Engineering, Faculty of Science and Engineering, Waseda University, 3-4-1, Okubo, Shinjuku, Tokyo 169-8555, Japan
[3] Waseda Research Institute for Science and Engineering, Faculty of Science and Engineering, Waseda University, 3-4-1 Okubo, Shinjuku, Tokyo 169-8555, Japan
[4] Institute for Advanced Research, Nagoya University, Furo, Chikusa, Nagoya 464-8602, Japan
[5] Department of Space, Earth, & Environment, Chalmers University of Technology, Chalmersplatsen 4 412 96 Gothenburg, Sweden
[6] Graduate School of Pure and Applied Sciences, University of Tsukuba, 1-1-1 Tennodai, Tsukuba, Ibaraki 305-8571, Japan
[7] Tomonaga Center for the History of the Universe, University of Tsukuba, 1-1-1 Tennodai, Tsukuba, Ibaraki 305-8571, Japan
[8] Center for Frontier Science, Chiba University, 1-33 Yayoi-cho, Inage-ku, Chiba 263-8522, Japan
[9] Institute for Cosmic Ray Research, The University of Tokyo, 5-1-5 Kashiwanoha, Kashiwa, Chiba 277-8582, Japan
[10] National Astronomical Observatory of Japan, 2-21-1 Osawa, Mitaka, Tokyo 181-8588, Japan
[11] The Graduate University for Advanced Studies (SOKENDAI), 2-21-1 Osawa, Mitaka, Tokyo 181-8588, Japan
[12] Kitami Institute of Technology, 165 Koen-cho, Kitami, Hokkaido 090-8507, Japan

Abstract

Porous interstellar medium (ISM) structure in galaxies at the epoch of reionization gives us a hint to understand what types of galaxies contribute to reionization. Although recent studies have pointed out the positive correlation between high ionizing photon escape fractions and high [O III] 88 μm/[C II] 158 μm ratios found in UV-luminous star-forming galaxies at $z > 6$ with the Atacama Large Millimeter/submillimeter Array, previous studies have paid little attention to the neutral gas porosity that allows ionizing photons to escape. Here we present a detailed analysis of a $z = 8.312$ Lyman break galaxy, MACS0416_Y1 with a high $L_{[O\ III]\ 88\ \mu m}/L_{[C\ II]\ 158\ \mu m}$ ratio (≈ 9) and dust continuum detection. We construct a multiphase ISM model incorporating the neutral gas covering fraction ($cov_{\rm PDR}$). The best-fit model reveals a $cov_{\rm PDR} \approx 25\%$, indicating that $\approx 75\%$ of the ionized gas region is exposed to intercloud space. We confirm that our conclusions hold even when varying star formation history, stellar age, gas/stellar metallicity, and carbon-to-oxygen abundance ratio. This finding meets one of the necessary conditions for galaxies to have a nonzero escape fraction of ionizing photons and supports recent studies that galaxies with a high [O III] 88 μm/[C II] 158 μm ratio, such as MACS0416_Y1, could contribute to cosmic reionization. Furthermore, the modeled H II region with the best-fitting parameters has a typical size ($D = 0.90$ pc) and gas density ($\log n_{\rm H,c}/{\rm cm}^{-3} = 2.7$) that are comparable to local compact H II regions. This suggests that the H II regions in MACS0416_Y1 are in an early evolutionary stage.

Unified Astronomy Thesaurus concepts: Galaxy evolution (594); Interstellar medium (847); Lyman-break galaxies (979)

1. Introduction

Chemically enriched, massive galaxy populations at the epoch of reionization (EoR) play a significant role in galaxy formation and evolution through active star formation and feedback (e.g., P. Behroozi et al. 2019). They offer unexpected insights into the early Universe, including the presence of abundant luminous galaxy populations at $z \gtrsim 10$ (e.g., A. J. Bunker et al. 2023; E. Curtis-Lake et al. 2023; Y. Harikane et al. 2024; S. Carniani et al. 2024; M. Castellano et al. 2024; J. A. Zavala et al. 2024) and overdensity regions serving as sites of metal enrichment (e.g., T. Hashimoto et al. 2023; T. Morishita et al. 2023; G. C. Jones et al. 2024b). These galaxies could also be dominant contributors to cosmic reionization under the late ionization scenario proposed by R. P. Naidu et al. (2020). This scenario has recently been supported by statistical analysis of Lyα damping

wings (H. Umeda et al. 2024) and the velocity offset of Lyα emission (M. Nakane et al. 2024) based on spectroscopic data from the James Webb Space Telescope (JWST).

The neutral gas phase, specifically the photodissociation region (PDR; D. J. Hollenbach & A. G. G. M. Tielens 1999; M. G. Wolfire et al. 2022), and/or the molecular gas phase are crucial for understanding the physical properties of the interstellar medium (ISM), including the escape of ionizing photons into intergalactic space. JWST observations of rest-frame ultraviolet (UV)/optical emission lines are not appropriate to reveal the physical properties of these gas phases since atoms/ions that radiate bright lines to be detectable even in high-z galaxies typically have higher ionization potentials than hydrogen (13.6 eV).[13] The rest-frame far-infrared (FIR) [C II] 158 μm emission-line and dust continuum observations with the Atacama Large Millimeter/submillimeter Array (ALMA) offer complementary insights (e.g., T. Hashimoto

---

[13] The ionization potential of sulfur (10.36 eV) is lower than that of hydrogen, but [S II] lines are not bright in PDR because collisions with electrons emit the lines (B. T. Draine 2011).

et al. 2023; S. Fujimoto et al. 2024). Dust grains absorb UV radiation from ionizing sources and reemit thermal continuum emission, making rest-frame FIR dust continuum emission a reliable tracer of dust-obscured star formation (e.g., P. Madau & M. Dickinson 2014; Y. Fudamoto et al. 2021; J. A. Zavala et al. 2021; H. S. B. Algera et al. 2023) and dust mass (e.g., Y. Tamura et al. 2019; T. J. L. C. Bakx et al. 2021; Y. Sugahara et al. 2021; J. Witstok et al. 2022; H. S. B. Algera et al. 2024b) in galaxies. The [C II] 158 μm is one of the primary coolants of the ISM in the FIR emission lines in the local Universe (e.g., S. C. Madden et al. 2013; T. Díaz-Santos et al. 2017; R. Herrera-Camus et al. 2018) and is widely used as a good tracer of global star formation (e.g., I. De Looze et al. 2011, 2014; R. Herrera-Camus et al. 2015) and the PDR (T. Díaz-Santos et al. 2017; D. Cormier et al. 2019). Taking advantage of its luminous nature, ALMA has routinely observed redshifted [C II] 158 μm toward galaxies at $z \geqslant 4.5$, including four ALMA large programs (ALPINE, O. Le Fèvre et al. 2020; REBELS, R. J. Bouwens et al. 2022; CRISTAL, R. Herrera–Camus et al 2025 ; ASPIRE[14]). These observations reveal that this emission line remains a good tracer of global star formation rates (SFRs) even at such high redshifts (e.g., D. Schaerer et al. 2020; L. Liang et al. 2024). In addition, J. Witstok et al. (2022) reported a galaxy at $z \sim 7$ for which [C II] 158 μm predominantly originates from PDRs based on the comparison between the [C II] and [N II] 205μm emission lines, which have similar critical densities but are emitted by ions with different ionization potentials.

The [O III] 88 μm line is known to be another brightest emission line in the local Universe (e.g., H. Takami et al. 1987; M. Mizutani et al. 2002; H. Matsuo et al. 2009; D. Cormier et al. 2015; R. Herrera-Camus et al. 2018). It is considered to trace ionized gas regions because of high ionization potential (35.1 eV). Since A. K. Inoue et al. (2016) reported a detection of redshifted [O III] 88 μm emission in a Lyα emitter (LAE) at $z = 7.21$ with ALMA, based on the model predictions in A. K. Inoue et al. (2014), subsequent studies have detected this line in UV-luminous star-forming galaxies (LAEs and Lyman break galaxies (LBGs); e.g., T. Hashimoto et al. 2018, 2019a; Y. Tamura et al. 2019; Y. Harikane et al. 2020; H. B. Akins et al. 2022; J. Witstok et al. 2022; S. Fujimoto et al. 2024), dusty star-forming galaxies (e.g., D. P. Marrone et al. 2018; K.-i. Tadaki et al. 2022; H. S. B. Algera et al. 2024b; T. J. L. C. Bakx et al. 2024), and quasars (e.g., F. Walter et al. 2018; T. Hashimoto et al. 2019b) at $z \gtrsim 6$. The luminosity ratios of [O III] 88 μm to [C II] 158 μm for UV-luminous star-forming galaxies at $z \gtrsim 6$ have been found to be $L_{\text{[O III]}}/L_{\text{[C II]}} \gtrsim 3$ (A. K. Inoue et al. 2016; T. Hashimoto et al. 2019a; N. Laporte et al. 2019; T. J. L. C. Bakx et al. 2020; S. Carniani et al. 2020; Y. Harikane et al. 2020; J. Witstok et al. 2022), which is higher than that observed in more massive and dusty galaxies at the same epoch ($L_{\text{[O III]}}/L_{\text{[C II]}} \lesssim 1.5$; e.g., D. P. Marrone et al. 2018; H. S. B. Algera et al. 2024b) and even in local low-metallicity dwarfs ($L_{\text{[O III]}}/L_{\text{[C II]}} \approx 2$; D. Cormier et al. 2015), with the exception of Pox 186 with a [O III] 88 μm/[C II] 158 μm ratio of $\gtrsim 10$ (N. Kumari et al. 2024).

The origins of such high $L_{\text{[O III]}}/L_{\text{[C II]}}$ ratios in galaxies at $z \gtrsim 6$ have been explored through both observational and numerical studies. Possible origins include the extraordinary

nature of ionizing sources (high ionization parameters, bursty star formation histories (SFHs), and top-heavy initial mass functions (IMFs)) and/or gas physical and chemical conditions (low carbon-to-oxygen abundance ratios, low covering fractions of a PDR surrounding the ionized gas region, and high Lyman continuum escape fractions), although observational biases such as strong cosmic microwave background (CMB) attenuation, spatially extended [C II] halos, and inclination effects might be the case (S. Arata et al. 2020; T. J. L. C. Bakx et al. 2020; S. Carniani et al. 2020; Y. Harikane et al. 2020; L. Vallini et al. 2021; H. Katz et al. 2022; L. Ramambason et al. 2022; Y. Sugahara et al. 2022; R. Ura et al. 2023; T. J. L. C. Bakx et al. 2024; S. Fujimoto et al. 2024; C. T. Nyhagen et al. 2024; A. Schimek et al. 2024).

The key to resolving the degeneracy between ionizing sources and gas physical conditions lies in performing more detailed modeling of the ISM properties. Notably, D. Cormier et al. (2019; see also L. Ramambason et al. 2022) developed a multiphase ISM model incorporating neutral gas "porosity" using photoionization code CLOUDY (G. J. Ferland et al. 2017). They estimated the ionization parameters, gas densities, and neutral gas porosity for the Herschel dwarf galaxy survey samples (S. C. Madden et al. 2013) based on FIR emission lines and dust continuum. They show that galaxies with lower metal abundances tend to have larger neutral gas porosity, suggesting that low metal dwarfs in the early Universe might have porous neutral gas and contribute to cosmic reionization. In general, applying their method to high-redshift galaxies is a challenging task because of the poorer observational constraints; however, for certain galaxies with detections of at least two FIR emission lines and dust continuum, it is possible to investigate these three parameters, i.e., the ionization parameter, the gas density, and the neutral gas porosity.

In this paper, we investigate the physical properties of the ISM in MACS0416_Y1 at $z = 8.312$, one of the LBGs with ALMA detections in [O III] 88 μm, [C II] 158 μm, and dust continuum, by comparing observations and photoionization models. We briefly describe the target in Section 2, and we explain our models in Section 3. We show the results for the modeling and discuss consistency with other observations in Section 4. In Section 5.1, we discuss a potential contribution of old stellar populations to the young ones from the spectral energy distribution (SED), and Section 5.2 presents the physical properties of the modeled H II region with the best-fit parameters. Section 5.3 discusses the systematic differences related to parameter selection in our model. Finally, we provide a summary of our results in Section 6. Throughout this paper, we adopted a spatially flat ΛCDM cosmology with the best-fit parameters derived from the Planck results (Planck Collaboration VI 2020), which are $\Omega_M = 0.310$, $\Omega_\Lambda = 0.690$, and $h = 0.677$.

2. Target: MACS0416_Y1

Our target, MACS0416_Y1 (hereafter Y1), was first found as a bright, Y-band dropout LBG (L. Infante et al. 2015; N. Laporte et al. 2015) and is moderately gravitationally magnified ($\mu_g = 1.43 \pm 0.04$[15]; R. Kawamata et al. 2016) by the foreground massive galaxy cluster MACS0416.1−2403.

---

[14] https://aspire-quasar.github.io/project-alma.html

[15] Recently two different groups reported revised estimates based on the new data, but they are completely different ($\mu_g = 1.21$ in Z. Ma et al. 2024, and $\mu_g = 1.60^{+0.01}_{-0.02}$ in A. Harshan et al. 2024). In this paper, we use the same factor to correct all luminosities, so which value is used does not affect the result.

Follow-up observations with ALMA identified the spectroscopic redshift to be $z = 8.312$ through the detection of the rest-frame FIR [O III] 88 μm and [C II] 158 μm emission lines (Y. Tamura et al. 2019; T. J. L. C. Bakx et al. 2020). The global [O III] 88 μm/[C II] 158 μm luminosity ratio is $\approx 9.3 \pm 2.6$ (T. J. L. C. Bakx et al. 2020), making it one of the galaxies with the highest luminosity ratios in the EoR. Even when correcting for the surface brightness dimming effect, the ratio remains high ($\approx 8 \pm 2$; S. Carniani et al. 2020).

The rest-frame 90 μm dust continuum emission was also detected (Y. Tamura et al. 2019), while it was not detected at either rest-frame 120 μm or 160 μm (T. J. L. C. Bakx et al. 2020). This suggests that the SED within the range of $90 \lesssim \lambda_{\rm rest}/\mu{\rm m} \lesssim 160$ is close to the Rayleigh–Jeans regime with a high dust temperature of $T_d \gtrsim 80$ K (T. J. L. C. Bakx et al. 2020; L. Sommovigo et al. 2022; Y. Fudamoto et al. 2023; H. S. B. Algera et al. 2024b; G. C. Jones et al. 2024a). Such a high T_d leads to a high infrared luminosity ($L_{\rm IR} \approx 1 \times 10^{12}$ L$_\odot$ under $T_d = 80$ K and a dust emissivity index $\beta_d = 2$), indicating that dust clouds are exposed to intense and hard UV radiation from young, compact star-forming regions. These conditions potentially result in the high [O III]/[C II] ratios observed in this galaxy.

Y. Tamura et al. (2023) presented the 300 pc scale high-resolution imaging of the [O III] 88 μm emission line and rest-frame 90 μm dust continuum emission. They compared the spatial distributions of [O III] 88 μm, dust continuum, and young stellar populations traced by the Hubble Space Telescope (HST)/F160W filter (rest-frame $\sim$1600 Å). They revealed that the [O III] 88 μm emission has three peaks likely associated with three young stellar components, while the dust continuum has two peaks distributed between the stellar clumps. Such spatial segregation on the subkiloparsec scale between young stellar and dust clumps implies that ionizing photons could escape into the intercloud space through channels of low dust attenuation regions. In addition, new high-resolution [C II] imaging has revealed multiple [C II] clumps in the velocity regime (T. J. L. C. Bakx et al. 2025, in preparation).

Moreover, JWST observations have recently revealed the rest-frame optical view of Y1. G. Desprez et al. (2024) presented the NIRCam images of eight bands taken as part of the CAnadian NIRISS Unbiased Cluster Survey (CANUCS; C. J. Willott et al. 2022). They performed the SED fitting for the entire galaxy system using those data and archival HST/WFC3 data with Dense Basis (K. G. Iyer et al. 2019) and Bagpipes (A. C. Carnall et al. 2018), and they estimated the stellar masses to be $\log(M_\star) \approx 8.5$–9.0.

Z. Ma et al. (2024) also showed NIRCam images of eight filters taken by Prime Extragalactic Areas for Reionization and Lensing Science (PEARLS; R. A. Windhorst et al. 2023). Utilizing these NIRCam data and HST/WFC3 data obtained by the Hubble Frontier Fields program, they performed the SED fitting with Bagpipes for the entire galaxy system. As a result, they found that Y1 is young (age ≈ 4.7 Myr) and in a starburst phase (SFR ≈ 160 M$_\odot$ yr^{-1}). It has a similar stellar mass ($M_\star \approx 7.7 \times 10^8$ M$_\odot$) to that obtained by G. Desprez et al. (2024) and a flat UV slope ($-1.8 \lesssim \beta_{\rm UV} \lesssim -1.0$) because of the dust extinction ($0.92 \lesssim A_V \lesssim 1.10$). In addition, they decomposed three UV-bright clumps and performed the SED fit to these three individual clumps, which showed similar stellar masses ($M_\star \sim 3.3 \times 10^8$ M$_\odot$) but were relatively
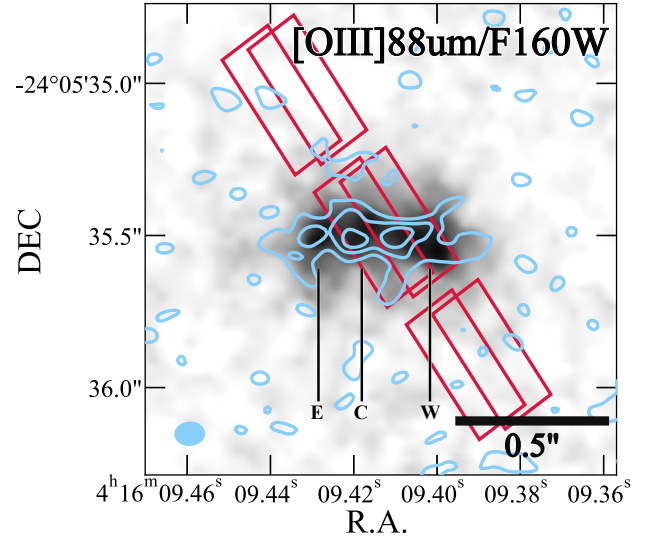
Figure 1. Rest-frame UV images (HST/F160W) with the contour of [O III] 88 μm moment 0 map reported in Y. Tamura et al. (2023). The contours are $(-2, 2, 4, 6, 8) \times \sigma$, where $1\sigma = 11$ mJy km s^{-1} beam^{-1}. We also overlaid the two slits used to obtain the spectrum with JWST/NIRSpec in A. Harshan et al. (2024). These two slits do not cover the eastern UV clump ("E" in the figure) as they reported. We find that the eastern peak of the [O III] 88 μm image is not covered by two slits as well. These findings suggest that their spectrum can underestimate the flux of the entire system by $\approx 2/3$.

diverse in other properties ($1.6 \lesssim \text{Age/Myr} \lesssim 10$, $30 \lesssim \text{SFR}/$M$_\odot$ yr$^{-1} \lesssim 200$, $0.6 \lesssim A_V \lesssim 1.2$, and $-2.5 \lesssim \beta_{\rm UV} \lesssim -1.0$). Moreover, they reported detection of the [O III] $\lambda\lambda 4960 + 5008$ and [O II] $\lambda\lambda 3727 + 3729$ emission lines with NIRCam wide-field slitless spectroscopy (PID 3538; E. Iani et al. 2023).

A. Harshan et al. (2024) presented a NIRSpec microshutter assembly (MSA) spectrum observed as a part of the CANUCS, in which a total of eight emission lines, including blended ones ([O II] $\lambda\lambda 3727+3729$ and Hγ + [O III] $\lambda 4364$), are evident. They predicted physical parameters such as electron temperature (T_e), gas-phase metallicity ($Z_{\rm gas}$), the ionization parameter (U), and electron density (n_e) by using obtained line ratios and PyNeb (V. Luridiana et al. 2015) or empirical relations between line ratios and physical parameters provided by Y. I. Izotov et al. (2006), L. J. Kewley et al. (2019), and D. C. Nicholls et al. (2020). They found that Y1 has comparable T_e ($\approx 18,000$ K) but is a more chemically evolved system ($Z_{\rm gas} \sim 15\%$ Z$_\odot$, $\log U \approx -2.5$) than other UV-bright galaxies at $z \sim 6$–8, which are confirmed by NIRSpec spectroscopy (e.g., D. Schaerer et al. 2022; A. J. Cameron et al. 2023). Electron density was measured to be ~ 100 cm^{-3} with the line ratio of [O III] 88 μm to [O III] $\lambda 5008$. A caveat includes that their results are based on the data taken within the two shutters covering only two of three UV clumps, indicating that they do not represent the total galaxy system (see Figure 1).

3. Methodology

3.1. Model Parameters

We used the photoionization code CLOUDY version 17.03 (G. J. Ferland et al. 2017) to construct the multiphase ISM model of Y1. We assume that the ISM consists of an ionized (H II region) and neutral gas (PDR) region (e.g., D. Cormier et al. 2019). The ISM is assumed to be spherically symmetric,

Table 1
Input Parameters of CLOUDY for Our Fiducial Model Grids

Fixed Parameters	
Stellar population	BPASS ver 2.0 (E. R. Stanway et al. 2016)
	Broken power-law IMF ($f(m) \propto m^\alpha$)
	$\alpha = -1.30$ for $0.1 \leqslant M_{\mathrm{star}}/M_\odot \leqslant 0.5$
	$\alpha = -2.35$ for $0.5 < M_{\mathrm{star}}/M_\odot \leqslant 100$
	Continuous star formation for 4 Myr,
	Stellar metallicity of $Z_{\mathrm{star}} = 0.2\,Z_\odot$
	(Y. Tamura et al. 2019)
	Including binary stars
Background radiation	CMB at $z = 8.3118$
	(Y. Tamura et al. 2019)
	Cosmic ray background
	(N. Indriolo et al. 2007)
Gas chemical composition	Solar one except for helium
	(N. Grevesse et al. 2010)
	Equation (1) for the helium abundance
	(B. A. Groves et al. 2004)
Grains model	ISM of Milky Way from CLOUDY
Gas-phase metallicity	$Z_{\mathrm{gas}} = 0.20\,Z_\odot (= Z_{\mathrm{star}})$
Density profile	$n_{\mathrm{H}} = n_{\mathrm{H},c} \times (1 + N(\mathrm{H})/10^{21}\ [\mathrm{cm}^{-2}])$
	(D. Cormier et al. 2019)
Stopping criteria	$\mathrm{H}^+/\mathrm{H_{tot}} = 0.01$ for H II region
	(N. P. Abel et al. 2005; T. Nagao et al. 2011)
	$A_V = 5$ mag for PDR
	(D. Cormier et al. 2019)
Dust temperature	80 K[a]
	(T. J. L. C. Bakx et al. 2020)

Varied Parameters	
$\log n_{\mathrm{H},c}/\mathrm{cm}^{-3}$	[1.0:4.0, 0.1 intervals]
$\log U$	[−4.0:0.0, 0.1 intervals]
cov_{PDR}[b]	[0.0:1.0, 0.01 intervals]

Notes.
[a] The dust temperature is not an input parameter of CLOUDY, but this significantly affects our fitting result via infrared luminosity. We adopt the dust temperature of 80 K in the fiducial model based on T. J. L. C. Bakx et al. (2020).
[b] cov_{PDR} is not an input parameter of CLOUDY.

with a central ionizing source completely surrounded by ionized gas. Our goal is to estimate the physical properties of the typical ISM in this galaxy by comparing our model with observations, where "typical" implies that this galaxy comprises numerous regions of such medium. In what follows, we explain the main input parameters for our fiducial model, which is also summarized in Table 1.

The incident spectrum consists of a stellar component and background radiation. The stellar component is modeled using the Binary Population and Spectral Synthesis (BPASS) code version 2.0 (J. J. Eldridge & E. R. Stanway 2016; E. R. Stanway et al. 2016). We employ a binary stellar model with the default IMF in the BPASS code, which has a shape of $f(m) \propto m^\alpha$ (m is the stellar mass), where the power-law indices, α, are $\alpha = -1.30$ and -2.35 within the stellar mass ranges of $m = 0.1$–$0.5\,M_\odot$ and 0.5–$100\,M_\odot$, respectively. We assume a continuous star formation for 4 Myr and a stellar metallicity of $0.20\,Z_\odot$, which were obtained by the rest-frame UV-to-FIR SED fits (Y. Tamura et al. 2019). As background radiation, we adopt only the CMB at $z = 8.3118$ (Y. Tamura et al. 2019), and for cosmic-ray background, we assume the

default CLOUDY assumptions (N. Indriolo et al. 2007) as a first-order approach.

We use the solar chemical composition for the gas-phase ISM (N. Grevesse et al. 2010). Still, for helium abundance, we adopt

$$\mathrm{He}/\mathrm{H} = 0.0737 + 0.0293 Z_{\mathrm{gas}}/Z_\odot \qquad (1)$$

(B. A. Groves et al. 2004; Y. Sugahara et al. 2022) to account for the big bang nucleosynthesis and stellar yields. We assume dust grains with the same size distribution and abundance pattern as the Milky Way, which is a default of CLOUDY. The gas-phase metallicity is assumed to be the same as the stellar one ($0.20\,Z_\odot$). We use the depth-dependent density profile following the previous study of the ISM modeling in low-metallicity environments (D. Cormier et al. 2019; L. Ramambason et al. 2022), given by

$$n_{\mathrm{H}} = n_{\mathrm{H},c} \times (1 + N(\mathrm{H})/10^{21}\,\mathrm{cm}^{-2}), \qquad (2)$$

where $n_{\mathrm{H},c}$ is the hydrogen volume density at the gas-illuminated face and $N(\mathrm{H})$ is the hydrogen column density at a given depth. In this formulation, the density is roughly constant within the H II region and increases along with hydrogen column density in the neutral gas (see also Figure 2 in D. Cormier et al. 2019). This represents the density profile as an intermediate choice between the two most common extreme regimes—constant pressure and constant density. We make two models with different stopping criteria to obtain intensities from PDRs and only the H II regions separated from PDRs. Our model calculations for PDRs were stopped where the V-band dust extinction, A_V magnitude, is five to cover the [C II] 158 μm emission sufficiently, following D. Cormier et al. (2019). In addition, we set a stopping criterion for the H II region as the depth where an ionized hydrogen fraction reaches 1% (N. P. Abel et al. 2005; T. Nagao et al. 2011). Note that we omit the density-bounded H II region (e.g., J. E. Beckman et al. 2000; K. Nakajima & M. Ouchi 2014) in our model to decrease the number of free parameters.

We investigated three free parameters to be obtained in our model: the hydrogen gas volume density at the gas-illuminated face $n_{\mathrm{H},c}$, the ionization parameter U at the gas-illuminated face, and the covering fraction of a PDR cov_{PDR}. Here cov_{PDR} is not an input parameter of CLOUDY, and we define this as the linear combination coefficient of the fraction of the H II region covered by a PDR. Our modeled luminosities are given by

$$L_{\mathrm{out}} = (1 - cov_{\mathrm{PDR}})L_{\mathrm{H\,II}} + cov_{\mathrm{PDR}}L_{\mathrm{H\,II+PDR}}, \qquad (3)$$

where L_{out} represents the final output luminosity, $L_{\mathrm{H\,II}}$ corresponds to the luminosity from the H II region completely uncovered by the PDR, and $L_{\mathrm{H\,II+PDR}}$ denotes the luminosity from the ISM entirely covered by the PDR. We generated a grid of models by varying the above three parameters within the range below: $\log n_{\mathrm{H},c}/\mathrm{cm}^{-3}$ in the range of $1.0 \leqslant \log n_{\mathrm{H},c}/\mathrm{cm}^{-3} \leqslant 4.0$ at 0.1 intervals, $\log U$ in the range of $-4.0 \leqslant \log U \leqslant 0.0$ at 0.1 intervals, and cov_{PDR} between zero (i.e., a H II region not covered by PDR at all) and unity (i.e., a completely covered H II region by PDR) at 0.01 intervals. These parameter spaces are consistent with previous studies (e.g., D. Cormier et al. 2019; Y. Harikane et al. 2020).

Table 2
Line and Continuum Luminosities Used in Our Modeling

$L_{\text{[O III] 88 }\mu m}$	$(1.29 \pm 0.39) \times 10^9 \, \text{L}_\odot$ [a]
$L_{\text{[C II] 158 }\mu m}$	$(1.42 \pm 0.23) \times 10^8 \, \text{L}_\odot$ [a]
L_{UV}	$(4.00 \pm 0.18) \times 10^{10} \, \text{L}_\odot$ [b]
L_{IR}	$9.8 \times 10^{11} \, \text{L}_\odot$ [c]

Notes.
[a] We calculate the line luminosities of [O III] 88 μm and [C II] 158 μm from the fluxes reported by Y. Tamura et al. (2019) and T. J. L. C. Bakx et al. (2020), respectively.
[b] We calculate the UV luminosity based on the photometry of HST/F140W (rest-frame 1500 Å) provided by Z. Ma et al. (2024).
[c] We obtain the infrared luminosity (rest-frame 8–1000 μm) based on the single dust continuum detection at $\lambda_{\text{rest}} \approx 90$ μm (Y. Tamura et al. 2019) and the simple modified blackbody with the dust emissivity index $\beta_d = 2.0$ and a dust temperature of 80 K from T. J. L. C. Bakx et al. (2020). We assume the error of the infrared luminosity to be 50%, corresponding to a dust temperature uncertainty of $\sim\pm10$ K.

3.2. Comparison with Observations

To compare our model with the observations, we need to scale the modeled luminosities to the observed ones. Throughout this paper, we use the magnification-corrected line and continuum luminosities, as shown in Table 2. Here we assume a magnification factor of 1.43 (R. Kawamata et al. 2016; Y. Tamura et al. 2019). We take the luminosity ratios instead of including the normalization factor as another free parameter. To minimize errors involved in the ratios, we choose the [O III] 88 μm luminosity with a better signal-to-noise ratio as the denominator.

We searched for the best-fit parameter sets by minimizing the χ^2, defined as

$$\chi^2 = \sum_{i=1}^{n_{\text{obs}}=3} \frac{(O_i - M_i)^2}{\sigma_i^2}, \qquad (4)$$

where O_i, M_i, and σ_i represent the observed and model-predicted luminosity ratios and the error in O_i for the ith pair of observables, respectively. To estimate the uncertainties of the best-fitting parameters, we employed a Monte Carlo method. Specifically, we repeated the fitting procedure 10,000 times, each time perturbing the observed ratios by adding random Gaussian noise with a standard deviation equal to the measured uncertainty (1σ) of each line ratio. From the resulting distribution of best-fit parameter values (i.e., those minimizing χ^2 in each realization), we adopted the median and $\pm$ 34th percentiles as the representative parameter values and their associated uncertainties.

4. Fiducial Model Results

4.1. Best-fit Parameters

Figure 2(a) shows the distributions of the best-fit parameter values obtained from each Monte Carlo realization, i.e., the parameter sets that yielded the minimum χ^2 in each run. In the histograms, the orange solid and dashed lines indicate the median and central 68th percentile intervals for each parameter, respectively. From these distributions, we derive the best-fitting parameters as $cov_{\text{PDR}} = 0.25^{+0.19}_{-0.14}$, $\log n_{\text{H},c}/\text{cm}^{-3} = 2.7^{+0.2}_{-0.55}$, and $\log U = -1.9 \pm 0.2$, respectively. In the following discussion, we use the median values of these distributions as
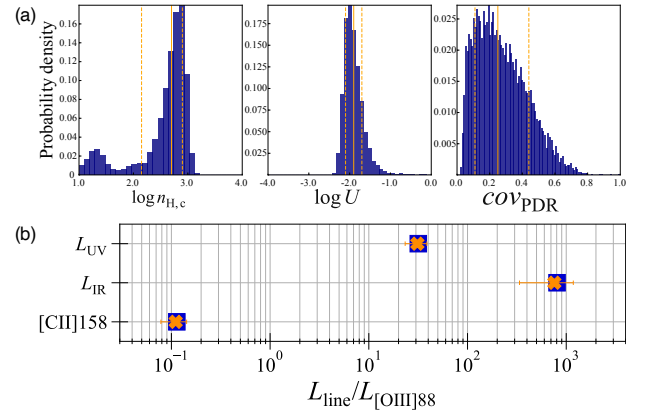
Figure 2. (a) The probability density distributions of each parameter obtained from a total of 10,000 Monte Carlo realizations. Orange solid and dashed lines correspond to the median and error as their 68th percentiles, and we define them as the best-fitting parameters. (b) Comparison between observed (orange crosses) and modeled (blue squares) luminosity ratios relative to [O III] 88 μm.

$(cov_{\text{PDR}} = 0.25, \log n_{\text{H},c} = 2.7, \log U = -1.9)$
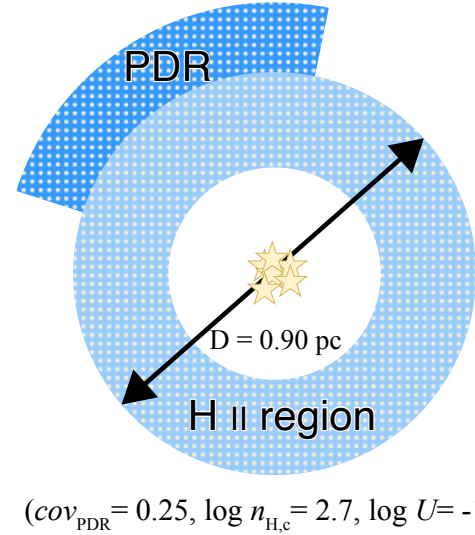
Figure 3. Schematic view of the ISM for the best-fit model parameter set.

representative parameters. Figure 2(b) compares the observed luminosity ratios with those predicted by the best-fitting model, showing good overall agreement. Figure 3 presents a two-dimensional schematic view of the "typical" ISM ionization structure derived from the best-fitting parameter set.

Our model predicts $cov_{\text{PDR}} \approx 25\%$, indicating that $\approx 75\%$ of the outer surface of a typical H II region is not covered by the PDR. In addition, the cov_{PDR} distribution clearly rules out a fully covered scenario ($cov_{\text{PDR}} = 1$). Recent studies have suggested that galaxies with a high [O III] 88 μm/[C II] 158 μm luminosity ratio could have high Lyman continuum escape fractions (H. Katz et al. 2022; R. Ura et al. 2023). Nonzero escape of ionizing photons requires an ionization structure of ISM where a fraction of the H II region is directly exposed to the intercloud space, implying a porous neutral gas structure or truncated structure with the edge of the ionization front. Our predicted low-cov_{PDR} aligns with this picture, supporting these previous findings. In summary, our result implies that ISM structures enabling ionizing photons to escape into the intercloud space exist even in relatively enriched galaxies with significant dust continuum detection during the EoR.

Our model suggests a gas density of $\approx 500\,\mathrm{cm^{-3}}$ for the H II region in Y1, which is consistent with the prediction by L. Vallini et al. (2021). This value is roughly two times higher than those estimated for $z \approx 7$ galaxies using [O III] 88 μm and other rest-frame FIR emission lines (Y. Sugahara et al. 2021; M. Killi et al. 2023). Our result is in agreement with the redshift evolution over $0 \lesssim z \lesssim 10$ of electron density estimated from the [O II] $\lambda\lambda 3727, 3729$ and [S II] $\lambda\lambda 6716, 6731$ doublet lines and the [O III] 88 μm/[O III] $\lambda 5008$ emission lines (Abdurro'uf et al. 2024).[16] They suggested that one of the origins of the redshift evolution is the metallicity evolution of galaxies from $\sim$500 Myr after the big bang. Y1 is estimated to have a metallicity of $\lesssim 0.20\,\mathrm{Z_\odot}$ (Y. Tamura et al. 2019; A. Harshan et al. 2024), similar to those of galaxy samples ($0.1 \lesssim Z/\mathrm{Z_\odot} \lesssim 0.4$) at $z \gtrsim 4$ used in Abdurro'uf et al. (2024). On the other hand, the targets with FIR line-based electron density measurement are estimated to be relatively metal enriched ($Z > 0.4\,\mathrm{Z_\odot}$ at $z \approx 7$; Y. Sugahara et al. 2021; M. Killi et al. 2023), implying that these higher-metallicity galaxies might not follow the same relation. Therefore, the metallicity difference between samples could explain the variations in the estimated electron densities.

Our estimated value for the electron density of Y1 is $\gtrsim 1.5$ times larger than that presented by A. Harshan et al. (2024). They used the combination of the three [O III] emission lines (rest-frame optical 4364 and 5008 Å from their observations and rest-frame FIR 88 μm from Y. Tamura et al. 2019) and PyNeb (V. Luridiana et al. 2015). As their NIRSpec/MSA slits covered only two of the three stellar clumps, as mentioned in Section 2, it is likely that the total intensities of the optical lines they observed are underestimated by a factor of $\approx 2/3$. If we simply assume that their flux measurements of optical [O III] emission lines account for 2/3 of the entire system, their n_e estimate could increase, giving an upper limit of $n_e \approx 500\,\mathrm{cm^{-3}}$, consistent with our estimate.

We obtained an ionization parameter of $\log U \approx -2.0$, which is roughly comparable to typical ionization parameters estimated for metal-poor UV-bright galaxies at $z \sim 6$–8 from the JADES survey (A. J. Cameron et al. 2023). In contrast, this is higher than the median value reported in the Herschel Dwarf Galaxy Survey (-2.4; D. Cormier et al. 2019), the average values of H II regions in our Galaxy (≈ -2.3; J. R. Rigby & G. H. Rieke 2004), and observations of super star clusters in M82 (N. M. Förster Schreiber et al. 2001; L. J. Smith et al. 2006). The higher ionization parameter found for Y1 reflects the observed high [O III] 88 μm/[C II] 158 μm luminosity ratio for Y1 compared to the local dwarf galaxies and star-forming regions.

Z. Ma et al. (2024) and A. Harshan et al. (2024) have reported two distinct values of $\log U = -1.60^{+0.14}_{-0.05}$ and $\log U = -2.48 \pm 0.30$, respectively. The simplest explanation of this discrepancy is in the difference between the tracers and the method they used. Z. Ma et al. (2024) estimated the ionization parameter based on the SED fits of the HST/JWST photometric data with `Bagpipes`, so their result depends on their assumption for nebular conditions and stellar population models. A. Harshan et al. (2024) calculated the line ratio of [O III] $\lambda 5008$/[O II] $\lambda\lambda 3727+3729$ (=O32) and used an analytical relationship between this line ratio and $\log U$

calibrated by L. J. Kewley et al. (2019). Note that this relation is valid in the range of $-3.98 \leqslant \log U \leqslant -2.48$, which is entirely different from the range Z. Ma et al. (2024) explored ($-2.5 < \log U < -0.5$). Our method involves [C II] 158 μm and fully simulates the multiphase ISM all the way from the ionized out to the neutral regions, which is in stark contrast to the method that Z. Ma et al. (2024) or A. Harshan et al. (2024) employed.

### 4.2. Predicted SED and Emission-line Luminosities

Figure 4(a) compares the best-fitting SED predicted by CLOUDY with the observed one, which allows for validation of our model. The predicted SED is normalized so as to match the HST/F140W photometry reported by Z. Ma et al. (2024). We find that the observed and modeled flux densities in the rest-frame far-UV (FUV) and JWST/F444W are in reasonable agreement. However, our model underestimates the flux densities at $2000 \lesssim \lambda_\mathrm{rest}/\mathrm{Å} \lesssim 4000$ (JWST/F200W, F277W, F356W, F410M) by $\sim$70%.

The possible attribution of this discrepancy is as follows: First, the dust attenuation law or grain size distribution we assumed in CLOUDY may differ from those of Y1. As mentioned in Section 3, our model employs the Milky Way–like extinction law, which is known to have an enhanced extinction at $\lambda_\mathrm{rest} \approx 2175$ Å and could reduce the FUV flux densities for a fixed A_V. This absorption feature is expected in the presence of interstellar growth of carbonaceous grains, but it is not likely for Y1, as it is too young to have substantial grain growth (Y. Tamura et al. 2019). If this is the case, adapting a dust extinction curve without the 2175 Å bump, such as the Calzetti law (D. Calzetti et al. 2000), could mitigate the discrepancy at F200W and F277W. This expectation aligns with the dust extinction curve for UV-luminous LBGs predicted from the infrared excess–β relation (R. A. A. Bowler et al. 2024; Y. Sugahara et al. 2025). In addition, it is in agreement with the predicted dust extinction curves for two star-forming galaxies at $z \sim 6$–8 by V. Markov et al. (2023), where they combine JWST/NIRSpec MSA data with the SED-fitting technique, including parameterizations of a dust attenuation law. The second possibility is the existence of an older stellar population in addition to the young stellar population in our CLOUDY model, which could redden the $\lambda_\mathrm{rest} \gtrsim 4000$ Å continuum spectrum. Although A. Harshan et al. (2024) did not report a significant Balmer break in the NIRSpec MSA spectrum, the presence of the older population has been proposed to explain the observed high dust mass and metallicity of Y1 (Y. Tamura et al. 2019). We test this scenario in Section 5.1.

Another indicator to validate our model is a series of the optical emission lines that are well constrained by recent JWST observations (A. Harshan et al. 2024). Our best-fitting model directly predicts the intrinsic optical line luminosities. They are scaled using the normalization factor we employed to match the model and observed SEDs (see Figure 4(a)). Then, they are compared with the extinction-corrected line luminosities, which were obtained from the JWST/NIRSpec MSA observations (Table 2 of A. Harshan et al. 2024) to be independent of the choice of extinction laws. Note that we correct the observed line luminosities by multiplying them by a factor of 1.5 since it is likely that the NIRSpec MSA observations lost $\approx 1/3$ of the total emission, as stated in Section 4.1. Figure 4(b) shows the line luminosities between

---

[16] They fit a power-law function to the relation between redshifts and electron densities, based on compiled measurements at $z = 0$–10 using those nebular line combinations.
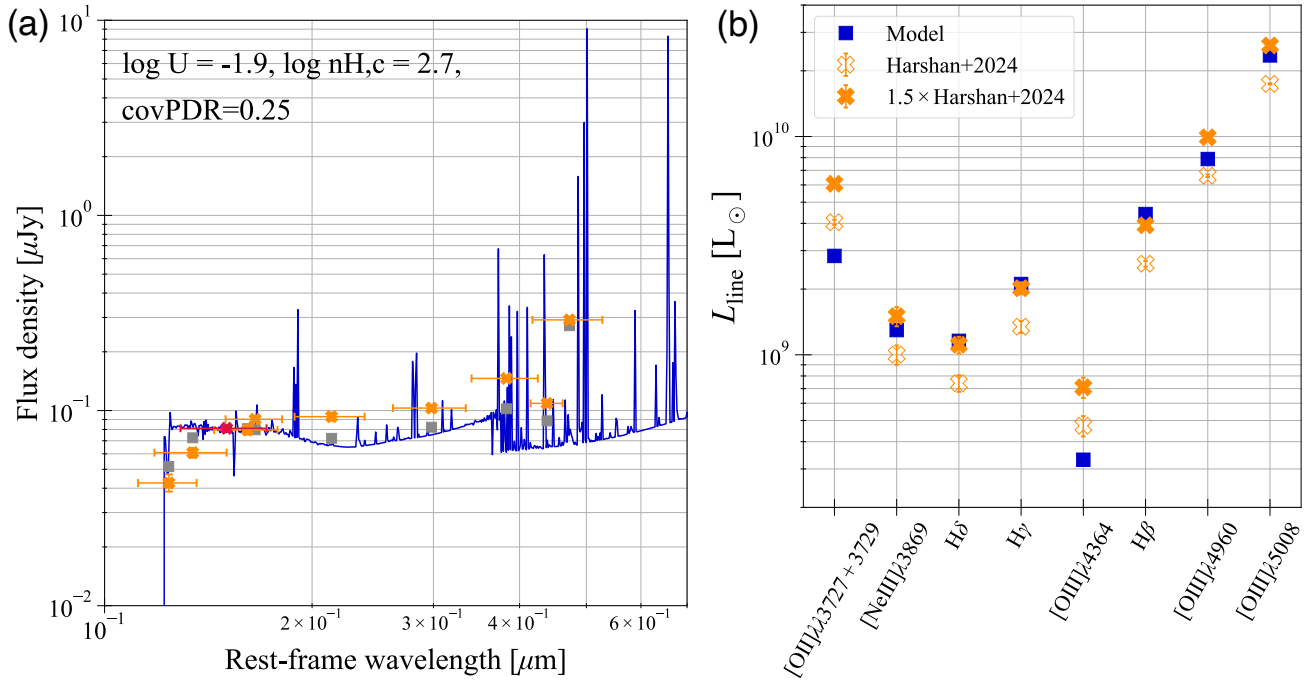
Figure 4. (a) Rest-frame UV-to-optical SED obtained from the CLOUDY model with the best-fit parameters (blue line) with modeled flux densities (gray squares) and extracted flux densities in Z. Ma et al. (2024) from HST and JWST observations (red and orange crosses, respectively). We used the red cross, the observed flux density of HST/F140W, to scale the model to the observations. (b) Comparison of rest-frame optical emission-line luminosities between our model with the best-fit parameters (blue squares) and observations (orange crosses). We correct the reported line fluxes in A. Harshan et al. (2024) for dust attenuation (orange open crosses). In addition, we consider luminosities with an additional factor of 1.5, which originates from the slit covering factor in A. Harshan et al. (2024; orange filled crosses). Our model reproduces the observed line luminosities of the Balmer lines (Hβ, Hγ, Hδ), [O III] $\lambda\lambda$4960, 5008, and [Ne III] λ3869. However, it underestimates the luminosities of the [O III] λ4364 and [O II] $\lambda\lambda$3727+3729 emission lines by approximately a factor of two.

our model (blue squares) and the observed spectrum (orange crosses). Without $1.5\times$ correction, our model overestimates most (six out of eight) of the optical line luminosities. With a $1.5\times$ correction applied, the predicted luminosities show improved agreement with six out of eight observed emission lines: Hβ, Hγ, Hδ, [O III] λ4960, [O III] λ5008, and [Ne III] λ3869.

However, our model underestimates the luminosities of the [O III] λ4364 and [O II] $\lambda\lambda$3727+3729 emission lines by approximately a factor of two. The upper energy levels of the [O III] λ4364 and [O III] λ5008 transitions are different, and the relative excitation rates to these levels depend on the electron temperature in the low-density regime ($n_e \lesssim 10^4\,\mathrm{cm}^{-3}$; D. E. Osterbrock & G. J. Ferland 2006). Since such densities are typical in local H II regions (K.-T. Kim & B.-C. Koo 2001), the line ratio between these transitions has been widely used as a diagnostic of T_e. A. Harshan et al. (2024) found an electron temperature of Y1 to be $T_e = 17{,}634 \pm 3900\,\mathrm{K}$ based on this line ratio and the best-fitting relation toward the modeled line ratio with the photoionization model obtained by D. C. Nicholls et al. (2020). The inferred T_e derived from the [O III] λ4364/[O III] λ5008 ratio of our best-fitting model is $T_e \approx 13{,}200\,\mathrm{K}$, which is lower than A. Harshan et al. (2024). We also find no model grid that reproduces such a high T_e.

The relatively low T_e predicted by our model may result from the relatively high gas-phase metallicity assumed in our CLOUDY calculations. The [O III] λ4364/[O III] λ5008 line ratio is sensitive to electron temperature, and because metals efficiently cool the gas, this ratio is negatively correlated with gas-phase metallicity (see D. E. Osterbrock & G. J. Ferland 2006; B. T. Draine 2011). Our model assumes a metallicity of

$Z = 0.20\,Z_\odot$ or $12 + \log(\mathrm{O/H}) = 7.99$ if we take the solar value of $12 + \log(\mathrm{O/H})_\odot = 8.69$ (N. Grevesse et al. 2010). In contrast, A. Harshan et al. (2024) estimated an oxygen abundance of $12 + \log(\mathrm{O/H}) = 7.8 \pm 0.2$ ($Z \approx 0.12\,Z_\odot$). Thus, adopting a lower metallicity in our model may mitigate the tension. Note that $Z \approx 0.12\,Z_\odot$ is even consistent with our previous estimate ($Z = 0.20^{+0.16}_{-0.18}\,Z_\odot$; Y. Tamura et al. 2019) within 1σ. On the other hand, Z. Ma et al. (2024) reported a solar metallicity, $Z \approx 1.0\,Z_\odot$, for the eastern component of Y1, which was dropped in the NIRSpec MSA spectroscopy of A. Harshan et al. (2024). The flux contribution from this metal-enriched eastern component would potentially reduce the total [O III] λ4364/[O III] λ5008 line ratio, mitigating the discrepancy.

The [O III] λ5008/[O II] $\lambda\lambda$3727+3729 emission-line ratio primarily depends on the ionization parameter when the metallicity difference is relatively small (e.g., a variation of $\Delta U \sim 0.3$ dex between 0.10 and 0.20 $Z_\odot$; L. J. Kewley & M. A. Dopita 2002). Therefore, the underestimation of the [O II] $\lambda\lambda$3727+3729 flux in our model is likely due to the high ionization parameter predicted by the best-fit solution. However, because of the limited number of observables, our modeling assumes a single-phase ionized gas component characterized by a single set of gas density and ionization parameter. As a result, the current model cannot fully reproduce the observed [O II] $\lambda\lambda$3727+3729 flux. To resolve this discrepancy, it may be necessary to introduce an additional ionized gas component with a lower ionization parameter (i.e., $\log U < -2.0$) beyond the framework of our fiducial model, which could account for the enhanced [O II] $\lambda\lambda$3727+3729 emission. Incorporating additional observational constraints in
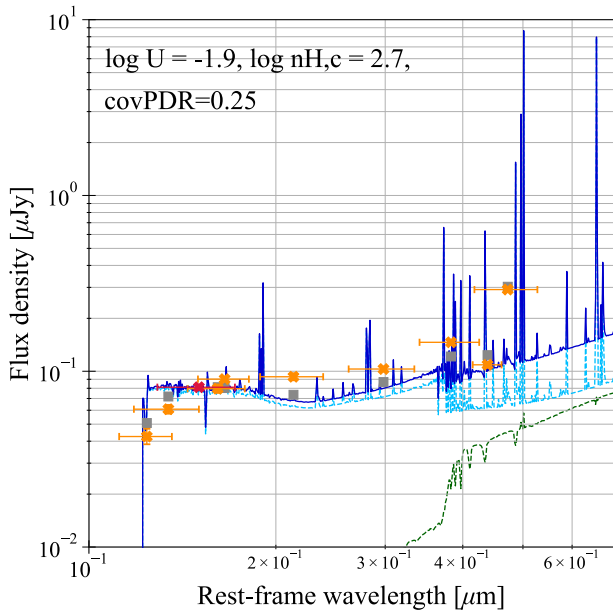
Figure 5. Rest-frame UV-to-optical SED model (blue line) in which an old stellar component made by a single starburst at 300 Myr ago (dashed green) is added to the best-fit SED model obtained in Section 4.2 (dashed light blue) with modeled flux densities (gray squares) and extracted flux densities in Z. Ma et al. (2024) from HST and JWST observations (red and orange crosses, respectively). We used the red cross, the observed flux density of HST/F140W, to scale the model to the observations. Including the additional contribution of the old stellar component makes the difference between models and observations at $\lambda_{\rm rest} \gtrsim 4000$ Å small.

future studies may allow for more detailed modeling of such multiphase ionized gas structures.

5. Discussions

5.1. Potential Coexistence of an Old Stellar Component

One of the potential solutions for reproducing the observed photometry at $\lambda_{\rm rest} \gtrsim 4000$ Å is an additional contribution from the underlying stellar component, which is older than the 4 Myr old component we used in the CLOUDY model. Indeed, Y. Tamura et al. (2019) suggested a possible contribution of the stellar population with a $\sim$300 Myr age for a necessary source of gas-phase metal and dust mass. In what follows, we test whether adding the old stellar population improves the discrepancy at $\lambda_{\rm rest} \gtrsim 4000$ Å. In CLOUDY calculations, we consider a stellar component that formed by a past single starburst 300 and 600 Myr ago at the time of $z = 8.31$, when the age of the Universe was $\approx$600 Myr. We assume the same ionization parameter and gas density as the best-fitting parameters of the fiducial model (see Section 4.1). The stellar SEDs are processed with the same CLOUDY setup as the fiducial model before being added to the young stellar component. The fractional contribution of an old stellar component to the young stellar component is determined by χ^2 fitting to the observed photometry, as shown with the orange crosses in Figure 4(a).

As a result, we find that the lowest-χ^2 values are almost the same in adding a stellar component of either 300 or 600 Myr ages ($\chi^2 = 194.34$ for 300 Myr and $\chi^2 = 193.00$ for 600 Myr). We adopt the case of adding the 300 Myr stellar population following Y. Tamura et al. (2019), where the young-to-old fractional contribution is 1.7:1 in the Paschen continuum

luminosity (3646–8204 Å). Figure 5 shows the model SEDs of young (light blue), old (green), and composite stellar populations (blue) with modeled (gray squares) and observed photometry (orange and red crosses). We find that the F410M photometry is improved, although it still fails to reproduce F356W. This is likely due to the fact that the emission-line contribution to F356W, such as [O II] $\lambda\lambda3727, 3729$, is significantly underestimated owing to a high ionization parameter, as we saw in Section 4.2. Adding a less ionized component is necessary for fully characterizing the ISM, which we leave for future works.

### 5.2. Physical Size and Morphology of a Typical H II Region

The spatial scale of a typical H II region would help one understand the evolutionary phase of the star formation in Y1. Although resolving individual H II regions is impossible, the nebular parameters, $n_{\rm H}$ and U, set the Strömgren sphere with a radius of $r_{\rm S}$, which can be used as a proxy for a spatial scale of the typical H II region of Y1. We derive a hydrogen gas density of $\log n_{{\rm H},c}/{\rm cm}^{-3} = 2.7$ and an ionization parameter of $\log U = -1.9$ as the physical properties of the typical ISM in Y1. In the CLOUDY code, $r_{\rm S}$ is defined as the point where the neutral hydrogen fraction reaches $H^0/H_{\rm tot} = 0.5$. Here we simply assume that $r_{\rm S}$ is the radius of the modeled H II region. One should note that the size of the H II region, in reality, includes the distance from the central ionizing source to the gas-illuminated face.

Our model estimates $r_{\rm S} = 0.45$ pc, corresponding to the H II region size of $D = 0.90$ pc in diameter. This size scale is as large as a compact H II region found in the Milky Way (e.g., S. Kurtz 2005; J. S. Urquhart et al. 2013), suggesting that the typical H II region in Y1 is in a relatively young evolutionary stage, consistent with its young stellar age ($\sim$4 Myr). In general, such a young H II region does not reach pressure equilibrium, which supports our initial assumption of the continuous density profile at the ionization front. The derived size of $D = 0.90$ pc and hydrogen density of $\log n_{{\rm H},c}/{\rm cm}^{-3} = 2.7$ follow the local size–density relation presented in K.-T. Kim & B.-C. Koo (2001).

Our model predicts two seemingly contradictory ISM properties: the porous neutral gas and the compact H II region that is generally thought to be embedded in a molecular cloud. K.-T. Kim & B.-C. Koo (2001) pointed out that most local ultracompact H II regions are likely associated with extended emissions. To explain its origin, they proposed a simple geometrical model (see Figure 8 of their study) in which central ionizing sources in an ultracompact H II region are born at the edge of a molecular cloud and are subsequently ionizing the lower-density side faster, making the extended emission associated with the ultracompact H II region. This picture is consistent with the porous geometry of neutral gas we depict in Y1 (Figure 3), suggesting the presence of multiple density components, which may be characterized by a similar photoionization model constrained with more nebular lines with a range of critical densities.

5.3. Systematics with Fixed Parameters

Due to the limited number of observables, we have to focus on only three parameters ($cov_{\rm PDR}$, $\log n_{{\rm H},c}$, $\log U$), with the other parameters fixed in our modeling. However, some of these fixed parameters could influence our conclusions
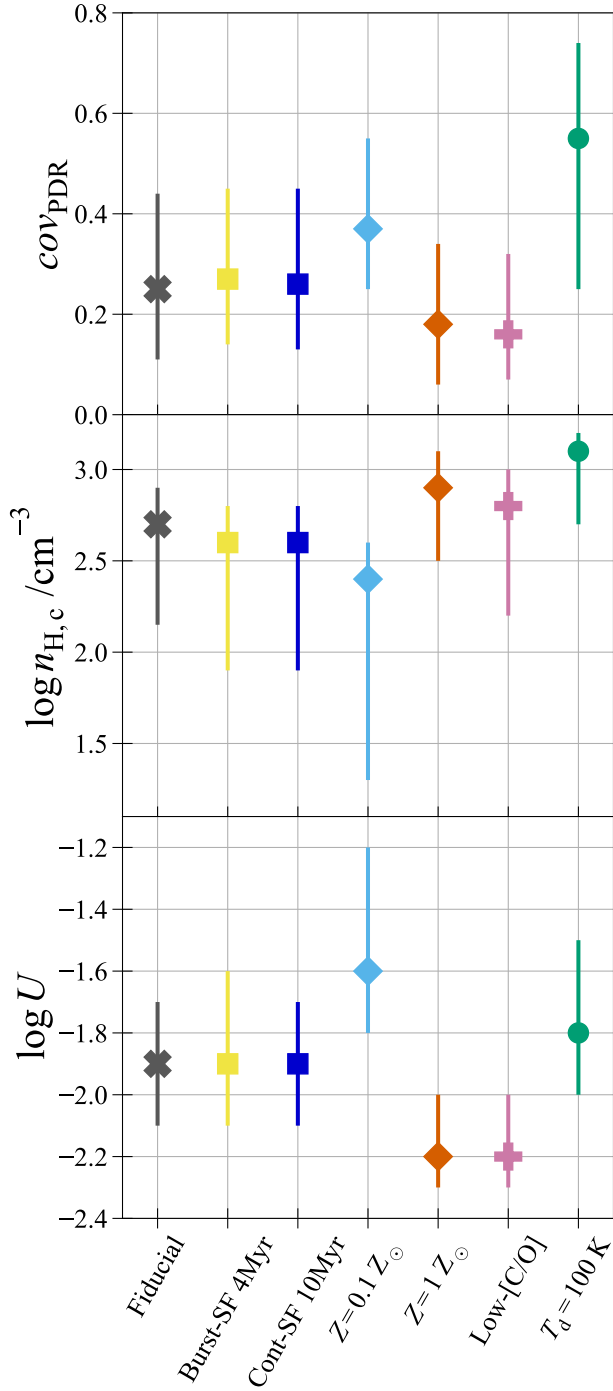
Figure 6. Comparison of the best-fitting values for the covering fraction (cov_{PDR}), gas density ($\log n_{H,c}/cm^{-3}$), and ionization parameter ($\log U$), with the central 68th percentile obtained from the same method used in Section 4.1. In addition to the fiducial model, six models with different assumptions are tested (see Section 5.3 for details about those models). Most of the results are consistent with the fiducial model. Although we find differences in the cases of lower Z ($Z = 0.10\,Z_\odot$) and higher-dust temperature (i.e., higher-infrared luminosity), the differences do not change our conclusion.

obtained from the fiducial model. In this part, we validate the reliability of our model predictions by changing parameters that are fixed in the fiducial model. Figure 6 summarizes the best-fit value with the central 68% confidence interval of each parameter predicted for a total of seven models, including the fiducial one. Below, we explain the details of the model parameters and the fitting results.
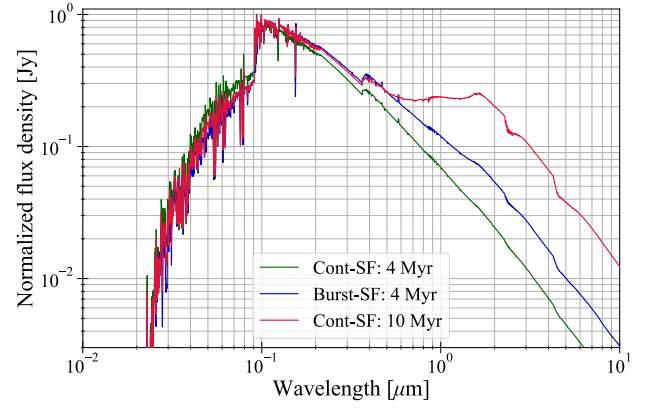
Figure 7. Comparison of normalized rest-frame UV-to-MIR SED of input stellar models. We find no significant difference between continuous and bursty SFH models of 4 Myr and also between the stellar age of 4 and 10 Myr. We assumed $\log n_{H,c}/cm^{-3} = 3.0$ and $\log U = -2.0$ for all SEDs.

SFH and Stellar Age. Our fiducial model adopts a continuous star formation of 4 Myr with the BPASS code. Here we check the effects on our model predictions by changing (i) SFH to a bursty one and (ii) the stellar age to 10 Myr following A. K. Inoue et al. (2014) and D. Cormier et al. (2019). Figure 7 compares the rest-frame UV-to-MIR input stellar SED among them, normalized to unity at the peak for all models. We find no significant difference in the spectral shape of the UV range among these three models, suggesting no significant change in our model results. The yellow and blue squares in Figure 6 correspond to the best-fit parameters for the bursty SFH of 4 Myr and constant SFH of 10 Myr, respectively. We find that the obtained best-fit parameters are consistent with each other; therefore, the differences in SFH and stellar ages do not change our model predictions.

Metallicity Dependence. We assumed that the gas and stellar metallicities of Y1 are the same, with $Z = 0.20\,Z_\odot$, based on the SED fit results shown by Y. Tamura et al. (2019) in our fiducial model. However, differences in metallicity generally impact line diagnostics (e.g., D. E. Osterbrock & G. J. Ferland 2006; T. Nagao et al. 2011). Here we test two cases: $Z = 0.10\,Z_\odot$, which is consistent with the prediction by A. Harshan et al. (2024) based on optical emission lines, and $Z = 1.0\,Z_\odot$, used as the highest-metallicity case for galaxies at $z \gtrsim 6$ in previous studies (e.g., Y. Harikane et al. 2020; Y. Sugahara et al. 2022). The light-blue and orange diamonds in Figure 6 represent the best-fit parameters with the central 68% confidence intervals for $Z = 0.10\,Z_\odot$ and $Z = 1.0\,Z_\odot$, respectively. In both cases, the predicted values for all parameters are consistent with the fiducial model within 1σ. However, we observe a trend indicating a shift in the estimated parameter ranges. For $Z = 1.0\,Z_\odot$, the best-fitting values of the ionization parameter and cov_{PDR} become lower, while the gas density is higher than in the fiducial model. Conversely, a higher cov_{PDR}, a higher ionization parameter, and a lower gas density are preferred in the case of $Z = 0.10\,Z_\odot$. A lower Z leads to a lower luminosity of [O III] 88 μm (Y. Harikane et al. 2020; S. Fujimoto et al. 2024), prompting the best-fitting values to compensate for it: a lower $\log n_{H,c}$ increases the luminosity of [O III] 88 μm as the gas density approaches or falls below the critical density of this line (510 cm^{-3} at $T_e = 10,000$ K; D. E. Osterbrock & G. J. Ferland 2006), and a higher $\log U$ increases the $L_{[O\,III]\,88\,\mu m}/L_{[C\,II]\,158\,\mu m}$ ratio (see also R. Ura et al. 2023), and vice versa. A higher $\log U$ also leads to a

higher UV luminosity, resulting in a slightly higher cov_{PDR} to keep $L_{UV}/L_{[O\,III]\ 88\ \mu m}$ constant by absorbing more UV continuum in the lower-Z case and vice versa. This test again confirms the importance of metallicity in characterizing the other nebular parameters. We should note that the estimated gas density for the $Z = 0.10\,Z_\odot$ model agrees with the electron density obtained by A. Harshan et al. (2024), but the estimated ionization parameter is higher than theirs. This result supports that Y1 may have additional low-ionized gas components other than our modeled one (see Section 4.2).

Carbon-to-oxygen Abundance Ratio. To explain high [O III]/[C II], the carbon-to-oxygen abundance ratio ([C/O]) is another critical indicator (H. Katz et al. 2022; C. T. Nyhagen et al. 2024). Here we estimate the physical properties for a lower [C/O] ratio than the solar value with a metallicity of $Z = 0.20\,Z_\odot$ using the scaling relation in M. A. Dopita et al. (2006),

$$[C/H] = 6.0 \times 10^{-5}(Z/Z_\odot) + 2.0 \times 10^{-4}(Z/Z_\odot)^2. \quad (5)$$

The obtained [C/O] is $\approx37\%$ of the solar value, consistent with the estimated value for a galaxy at $z = 6.23$ based on JWST/NIRSpec measurements (T. Jones et al. 2023). The pink plus sign in Figure 6 shows the modeling result. Although the cov_{PDR} and $\log U$ are slightly lower than the fiducial model to recover the reduced [C II] 158 μm flux, they are consistent with each other. Therefore, we find that the difference in [C/O] does not change our model results.

Dust Temperature Uncertainty. Tightly constraining the dust temperatures of high-z galaxies is generally difficult owing to the limited number of rest-frame FIR continuum measurement points (e.g., H. Inami et al. 2022; J. Witstok et al. 2022). So far, this has only been achieved in two cases, A1689-zD1 at $z = 7.13$ (T. J. L. C. Bakx et al. 2021; H. B. Akins et al. 2022) and REBELS-25 at $z = 7.31$ (H. S. B. Algera et al. 2024a). Uncertainty in the dust temperature leads to uncertainty in infrared luminosity. For Y1, several studies consistently show a high T_d of $T_d \gtrsim 80$ K (T. J. L. C. Bakx et al. 2020; L. Sommovigo et al. 2022; Y. Fudamoto et al. 2023; H. S. B. Algera et al. 2024b) with various methods. As the infrared luminosity increases with T_d given a fixed dust emissivity index β_d, it is essential to check the impact of a higher T_d than the fiducial model of $T_d = 80$ K on our results. Here we investigate the case of $T_d = 100$ K, which corresponds to $L_{IR} = 2.3 \times 10^{12}\,L_\odot$. The green circle in Figure 6 shows the best-fit parameters for this scenario. Although the obtained $cov_{PDR} = 0.55$ is consistent with the fiducial model owing to the large error, it is the largest value in explored space. In addition, the ionization parameter does not change, unlike in the case of low metallicity. This result highlights the importance of dust continuum observations toward galaxies at the EoR in the (sub)millimeter regime to constrain the neutral gas covering fraction. Even in this case, the solution of $cov_{PDR} = 1$ is rejected, meaning that our conclusion that a part of the H II region is exposed to the intercloud space remains unchanged.

6. Summary

We have investigated the physical properties of the typical ISM of MACS0416_Y1 at $z = 8.312$ by combining ALMA, HST, and JWST observations with photoionization models, taking into account the neutral gas porosity. The median with

error represented by 68th percentiles is $cov_{PDR} = 0.25^{+0.19}_{-0.14}$, $\log n_{H,c}/cm^{-3} = 2.7^{+0.2}_{-0.55}$, and $\log U = -1.9 \pm 0.2$, respectively. cov_{PDR} of ≈0.25 means that $\sim75\%$ of the outer surface of a typical H II region is exposed to the intercloud space. This porous neutral gas structure meets one of the requirements for nonzero escape fractions, suggesting that galaxies similar to Y1, with high-[O III]/[C II] ratios, could contribute to the cosmic reionization.

We predict the rest-frame optical SED and line luminosities of Y1 based on the best-fitting parameter sets and compare them with recent observations by JWST. As a result, we could roughly reproduce the observed SED. However, our model underestimates the observed photometry at $2000 \lesssim \lambda_{rest}/$ Å $\lesssim 4000$ and luminosities of [O III] $\lambda4364$ and [O II] $\lambda\lambda3727 + 3729$ emission lines by half. The discrepancies in F200W and F277W filters can be explained by the significant bump at $\lambda_{rest} \approx 2175$ Å in the assumed dust extinction law of the Milky Way. The discrepancy in F410M can be explained by additional contributions of a 300 Myr old stellar population. However, our model still underestimates the photometry of F356W even in adding such old stellar populations, indicating that [O II] $\lambda\lambda3727+3729$ emission lines significantly impact that photometry. Therefore, we need to consider an additional ionized gas component with a low ionization parameter to explain them consistently.

We characterize the size of the typical H II region in Y1 with the best-fit parameters by assuming that the size D of the H II region equals $D = 2r_S$, where r_S is the Strömgren radius. We find $D = 0.90$ pc, corresponding to the size of local compact H II regions. The result indicates that the typical H II region in Y1 is in a relatively young evolutionary phase. This finding, along with the low cov_{PDR}, suggests that the central ionizing sources in H II regions were born at the edge of the molecular clump and have begun ionizing the low-density side.

In the fiducial model, we fixed physical parameters other than cov_{PDR}, $\log n_{H,c}$, and $\log U$ owing to the limited number of observables, which are the [O III] 88μm, the [C II] 158μm, the UV, and the infrared luminosities. As a result of our tests in cases where these fixed parameters are changed, we found that different metallicity ($Z = 0.10\,Z_\odot$ and $Z = 1.0\,Z_\odot$) and higher dust temperature ($T_d = 100$ K) cases impact our model results. In particular, higher T_d likely provides a significantly higher cov_{PDR} solution, indicating that dust continuum observations by (sub)millimeter facilities are crucial for constraining the neutral gas porosity. However, even in this case, our conclusion that the typical ISM in Y1 has a porous neutral gas structure remains unchanged.

This kind of research has been limited to the local Universe. However, ALMA has opened a new window to high-z galaxies with redshifted rest-frame FIR emission-line observations. These rich data allow us to extend this research to other galaxies and investigate the cov_{PDR} for EoR. In addition, JWST has provided us with data on the rest-frame UV-to-optical regimes for $z > 6$ galaxies. By taking advantage of joint observations from ALMA and JWST, we can construct more complex models, such as multicomponent H II regions. In the upcoming years, we aim to start rest-frame FIR emission-line observations toward $z > 8$ galaxies in the northern hemisphere using a new wideband (sub)millimeter receiver, FINER (Y. Tamura et al. 2024), that will be mounted on the Large Millimeter Telescope (D. H. Hughes et al. 2020) in México.

This will offer further opportunities to combine research with rest-frame UV-to-optical and FIR observations.

Acknowledgments

ORCID iDs

Masato Hagimoto ● https://orcid.org/0000-0001-8083-5814
Yoichi Tamura ● https://orcid.org/0000-0003-4807-8117
Akio K. Inoue ● https://orcid.org/0000-0002-7779-8677
Hideki Umehata ● https://orcid.org/0000-0003-1937-0573
Tom J. L. C. Bakx ● https://orcid.org/0000-0002-5268-2221
Takuya Hashimoto ● https://orcid.org/0000-0002-0898-4038
Ken Mawatari ● https://orcid.org/0000-0003-4985-0201
Yuma Sugahara ● https://orcid.org/0000-0001-6958-7856
Yoshinobu Fudamoto ● https://orcid.org/0000-0001-7440-8832
Yuichi Harikane ● https://orcid.org/0000-0002-6047-430X
Hiroshi Matsuo ● https://orcid.org/0000-0003-3278-2484
Akio Taniguchi ● https://orcid.org/0000-0002-9695-6183

References

Abdurro'uf, Larson, R. L., Coe, D., et al. 2024, ApJ, 973, 47
Abel, N. P., Ferland, G. J., Shaw, G., & van Hoof, P. A. M. 2005, ApJS, 161, 65
Akins, H. B., Fujimoto, S., Finlator, K., et al. 2022, ApJ, 934, 64
Algera, H. S. B., Inami, H., De Looze, I., et al. 2024a, MNRAS, 533, 3098
Algera, H. S. B., Inami, H., Oesch, P. A., et al. 2023, MNRAS, 518, 6142
Algera, H. S. B., Inami, H., Sommovigo, L., et al. 2024b, MNRAS, 527, 6867
Arata, S., Yajima, H., Nagamine, K., Abe, M., & Khochfar, S. 2020, MNRAS, 498, 5541
Astropy Collaboration, Price-Whelan, A. M., Lim, P. L., et al. 2022, ApJ, 935, 167
Astropy Collaboration, Price-Whelan, A. M., Sipőcz, B. M., et al. 2018, AJ, 156, 123
Astropy Collaboration, Robitaille, T. P., Tollerud, E. J., et al. 2013, A&A, 558, A33
Bakx, T. J. L. C., Algera, H. S. B., Venemans, B., et al. 2024, MNRAS, 532, 2270
Bakx, T. J. L. C., Sommovigo, L., Carniani, S., et al. 2021, MNRAS, 508, L58
Bakx, T. J. L. C., Tamura, Y., Hashimoto, T., et al. 2020, MNRAS, 493, 4294
Beckman, J. E., Rozas, M., Zurita, A., Watson, R. A., & Knapen, J. H. 2000, AJ, 119, 2728
Behroozi, P., Wechsler, R. H., Hearin, A. P., & Conroy, C. 2019, MNRAS, 488, 3143
Bouwens, R. J., Smit, R., Schouws, S., et al. 2022, ApJ, 931, 160
Bowler, R. A. A., Inami, H., Sommovigo, L., et al. 2024, MNRAS, 527, 5808
Bunker, A. J., Saxena, A., Cameron, A. J., et al. 2023, A&A, 677, A88
Calzetti, D., Armus, L., Bohlin, R. C., et al. 2000, ApJ, 533, 682
Cameron, A. J., Saxena, A., Bunker, A. J., et al. 2023, A&A, 677, A115
Carnall, A. C., McLure, R. J., Dunlop, J. S., & Davé, R. 2018, MNRAS, 480, 4379
Carniani, S., Ferrara, A., Maiolino, R., et al. 2020, MNRAS, 499, 5136
Carniani, S., Hainline, K., D'Eugenio, F., et al. 2024, Natur, 633, 318
Castellano, M., Napolitano, L., Fontana, A., et al. 2024, ApJ, 972, 143
Cormier, D., Abel, N. P., Hony, S., et al. 2019, A&A, 626, A23
Cormier, D., Madden, S. C., Lebouteiller, V., et al. 2015, A&A, 578, A53
Curtis-Lake, E., Carniani, S., Cameron, A., et al. 2023, NatAs, 7, 622
De Looze, I., Baes, M., Bendo, G. J., Cortese, L., & Fritz, J. 2011, MNRAS, 416, 2712
De Looze, I., Cormier, D., Lebouteiller, V., et al. 2014, A&A, 568, A62
Desprez, G., Martis, N. S., Asada, Y., et al. 2024, MNRAS, 530, 2935
Díaz-Santos, T., Armus, L., Charmandaris, V., et al. 2017, ApJ, 846, 32
Dopita, M. A., Fischera, J., Sutherland, R. S., et al. 2006, ApJS, 167, 177
Draine, B. T. 2011, Physics of the Interstellar and Intergalactic Medium (Princeton, NJ: Princeton Univ. Press)
Eldridge, J. J., & Stanway, E. R. 2016, MNRAS, 462, 3302
Ferland, G. J., Chatzikos, M., Guzmán, F., et al. 2017, RMxAA, 53, 385, https://arxiv.org/abs/1705.10877
Förster Schreiber, N. M., Genzel, R., Lutz, D., Kunze, D., & Sternberg, A. 2001, ApJ, 552, 544
Fudamoto, Y., Inoue, A. K., & Sugahara, Y. 2023, MNRAS, 521, 2962
Fudamoto, Y., Oesch, P. A., Schouws, S., et al. 2021, Natur, 597, 489
Fujimoto, S., Ouchi, M., Nakajima, K., et al. 2024, ApJ, 964, 146
Grevesse, N., Asplund, M., Sauval, A. J., & Scott, P. 2010, Ap&SS, 328, 179
Groves, B. A., Dopita, M. A., & Sutherland, R. S. 2004, ApJS, 153, 9
Harikane, Y., Nakajima, K., Ouchi, M., et al. 2024, ApJ, 960, 56
Harikane, Y., Ouchi, M., Inoue, A. K., et al. 2020, ApJ, 896, 93
Harris, C. R., Millman, K. J., van der Walt, S. J., et al. 2020, Natur, 585, 357
Harshan, A., Tripodi, R., Martis, N. S., et al. 2024, ApJL, 977, L36
Hashimoto, T., Álvarez-Márquez, J., Fudamoto, Y., et al. 2023, ApJL, 955, L2
Hashimoto, T., Inoue, A. K., Mawatari, K., et al. 2019a, PASJ, 71, 71
Hashimoto, T., Inoue, A. K., Tamura, Y., et al. 2019b, PASJ, 71, 109
Hashimoto, T., Laporte, N., Mawatari, K., et al. 2018, Natur, 557, 392
Herrera-Camus, R., Bolatto, A. D., Wolfire, M. G., et al. 2015, ApJ, 800, 1
Herrera-Camus, R., Sturm, E., Graciá-Carpio, J., et al. 2018, ApJ, 861, 94
Herrera–Camus, R., González–López, J., Förster Schreiber, N., et al. 2025, A&A, 699, A80
Hollenbach, D. J., & Tielens, A. G. G. M. 1999, RvMP, 71, 173
Hoyer, S., & Hamman, J. 2016, JORS, 5

Hughes, D. H., Schloerb, F. P., Aretxaga, I., et al. 2020, Proc. SPIE, 11445, 1144522

Hunter, J. D. 2007, CSE, 9, 90

Iani, E., Annunziatella, M., Bartosch Caminha, G., et al. 2023, Unveiling the properties of high-redshift low/intermediate-mass galaxies in Lensing fields with NIRCam Wide Field Slitless Spectroscopy, JWST Proposal. Cycle 2 #3538, STScI

Inami, H., Algera, H. S. B., Schouws, S., et al. 2022, MNRAS, 515, 3126

Indriolo, N., Geballe, T. R., Oka, T., McCall, B. J., et al. 2007, ApJ, 671, 1736

Infante, L., Zheng, W., Laporte, N., et al. 2015, ApJ, 815, 18

Inoue, A. K., Shimizu, I., Tamura, Y., et al. 2014, ApJL, 780, L18

Inoue, A. K., Tamura, Y., Matsuo, H., et al. 2016, Sci, 352, 1559

Iyer, K. G., Gawiser, E., Faber, S. M., et al. 2019, ApJ, 879, 116

Izotov, Y. I., Stasińska, G., Meynet, G., Guseva, N. G., & Thuan, T. X. 2006, A&A, 448, 955

Jones, G. C., Übler, H., Perna, M., et al. 2024b, A&A, 682, A122

Jones, G. C., Witstok, J., Concas, A., & Laporte, N. 2024a, MNRAS, 529, L1

Jones, T., Sanders, R., Chen, Y., et al. 2023, ApJL, 951, L17

Katz, H., Rosdahl, J., Kimm, T., et al. 2022, MNRAS, 510, 5603

Kawamata, R., Oguri, M., Ishigaki, M., Shimasaku, K., & Ouchi, M. 2016, ApJ, 819, 114

Kewley, L. J., & Dopita, M. A. 2002, ApJS, 142, 35

Kewley, L. J., Nicholls, D. C., & Sutherland, R. S. 2019, ARA&A, 57, 511

Killi, M., Watson, D., Fujimoto, S., et al. 2023, MNRAS, 521, 2526

Kim, K.-T., & Koo, B.-C. 2001, ApJ, 549, 979

Kumari, N., Smit, R., Leitherer, C., et al. 2024, MNRAS, 529, 781

Kurtz, S. 2005, in Massive Star Birth: A Crossroads of Astrophysics, ed. R. Cesaroni, M. Felli, E. Churchwell, & M. Walmsley (Cambridge: Cambridge Univ. Press)

Laporte, N., Katz, H., Ellis, R. S., et al. 2019, MNRAS, 487, L81

Laporte, N., Streblyanska, A., Kim, S., et al. 2015, A&A, 575, A92

Le Fèvre, O., Béthermin, M., Faisst, A., et al. 2020, A&A, 643, A1

Liang, L., Feldmann, R., Murray, N., et al. 2024, MNRAS, 528, 499

Lotz, J. 2013, HST Frontier Fields ("FRONTIER"), STScI/MAST, doi:10.17909/T9KK5N

Luridiana, V., Morisset, C., & Shaw, R. A. 2015, A&A, 573, A42

Ma, Z., Sun, B., Cheng, C., et al. 2024, ApJ, 975, 87

Madau, P., & Dickinson, M. 2014, ARA&A, 52, 415

Madden, S. C., Rémy-Ruyer, A., Galametz, M., et al. 2013, PASP, 125, 600

Markov, V., Gallerani, S., Pallottini, A., et al. 2023, A&A, 679, A12

Marrone, D. P., Spilker, J. S., Hayward, C. C., et al. 2018, Natur, 553, 51

Matsuo, H., Arai, T., Nitta, T., & Kosaka, A. 2009, in ASP Conf. Ser. 418, AKARI, a Light to Illuminate the Misty Universe, ed. T. Onaka, G. J. White, T. Nakagawa, & I. Yamamura (San Francisco, CA: ASP), 451

McKinney, W. 2010, in Proc. 9th Python in Science Conf. 56, ed. S. van der Walt & J. Millman, 56

Mizutani, M., Onaka, T., & Shibai, H. 2002, A&A, 382, 610

Morishita, T., Roberts-Borsani, G., Treu, T., et al. 2023, ApJL, 947, L24

Nagao, T., Maiolino, R., Marconi, A., & Matsuhara, H. 2011, A&A, 526, A149

Naidu, R. P., Tacchella, S., Mason, C. A., et al. 2020, ApJ, 892, 109

Nakajima, K., & Ouchi, M. 2014, MNRAS, 442, 900

Nakane, M., Ouchi, M., Nakajima, K., et al. 2024, ApJ, 967, 28

Nicholls, D. C., Kewley, L. J., & Sutherland, R. S. 2020, PASP, 132, 033001

Nyhagen, C. T., Schimek, A., Cicone, C., Decataldo, D., & Shen, S. 2024, arXiv:2410.18471

Osterbrock, D. E., & Ferland, G. J. 2006, Astrophysics of Gaseous Nebulae and Active Galactic Nuclei (Mill Valley, CA: Univ. Science Books)

Planck Collaboration VI. 2020, A&A, 641, A6

Ramambason, L., Lebouteiller, V., Bik, A., et al. 2022, A&A, 667, A35

Rigby, J. R., & Rieke, G. H. 2004, ApJ, 606, 237

Schaerer, D., Ginolfi, M., Béthermin, M., et al. 2020, A&A, 643, A3

Schaerer, D., Marques-Chaves, R., Barrufet, L., et al. 2022, A&A, 665, L4

Schimek, A., Cicone, C., Shen, S., et al. 2024, A&A, 687, L10

Smith, L. J., Westmoquette, M. S., Gallagher, J. S., et al. 2006, MNRAS, 370, 513

Sommovigo, L., Ferrara, A., Pallottini, A., et al. 2022, MNRAS, 513, 3122

Stanway, E. R., Eldridge, J. J., & Becker, G. D. 2016, MNRAS, 456, 485

Sugahara, Y., Álvarez-Márquez, J., Hashimoto, T., et al. 2025, ApJ, 981, 135

Sugahara, Y., Inoue, A. K., Fudamoto, Y., et al. 2022, ApJ, 935, 119

Sugahara, Y., Inoue, A. K., Hashimoto, T., et al. 2021, ApJ, 923, 5

Tadaki, K.-i., Tsujita, A., Tamura, Y., et al. 2022, PASJ, 74, L9

Takami, H., Maihara, T., Mizutani, K., et al. 1987, PASP, 99, 832

Tamura, Y., Bakx, T. J. L. C., Inoue, A. K., et al. 2023, ApJ, 952, 9

Tamura, Y., Mawatari, K., Hashimoto, T., et al. 2019, ApJ, 874, 27

Tamura, Y., Sakai, T., Kawabe, R., et al. 2024, Proc. SPIE, 13102, 131020G

Umeda, H., Ouchi, M., Nakajima, K., et al. 2024, ApJ, 971, 124

Ura, R., Hashimoto, T., Inoue, A. K., et al. 2023, ApJ, 948, 3

Urquhart, J. S., Thompson, M. A., Moore, T. J. T., et al. 2013, MNRAS, 435, 400

Vallini, L., Ferrara, A., Pallottini, A., Carniani, S., & Gallerani, S. 2021, MNRAS, 505, 5543

Virtanen, P., Gommers, R., Oliphant, T. E., et al. 2020, NatMe, 17, 261

Walter, F., Riechers, D., Novak, M., et al. 2018, ApJL, 869, L22

Willott, C. J., Doyon, R., Albert, L., et al. 2022, PASP, 134, 025002

Windhorst, R. A., Cohen, S. H., Jansen, R. A., et al. 2023, AJ, 165, 13

Witstok, J., Smit, R., Maiolino, R., et al. 2022, MNRAS, 515, 1751

Wolfire, M. G., Vallini, L., & Chevance, M. 2022, ARA&A, 60, 247

Zavala, J. A., Casey, C. M., Manning, S. M., et al. 2021, ApJ, 909, 165

Zavala, J. A., Castellano, M., Akins, H. B., et al. 2024, NatAs, 9, 155